PHYSICAL REVIEW APPLIED **22,** 014037 (2024)

# Nonreciprocal spin-wave beam transport in a metallized T-shaped magnonic junction

A.A. Martyshkin,[1,*] S.E. Sheshukova,[1] F.Y. Ogrin,[2,3] E.H. Lock,[4] D.V. Romanenko,[1] S.A. Nikitov,[5] and A.V. Sadovnikov[1]

[1] *Laboratory "Magnetic Metamaterials", Saratov State University, Saratov 410012, Russia*
[2] *School of Physics and Astronomy, University of Exeter, Exeter EX4 4QL, United Kingdom*
[3] *MaxLLG Ltd., United Kingdom*
[4] *Kotel'nikov Instutute of Radio Engineering and Electronics of RAS (Fryazino Branch), Vvedensky Square 1, Fryazino, Moscow Region 141190, Russia*
[5] *Kotel'nikov Institute of Radio-Engineering and Electronics of RAS, Mokhovaya Street 11, Building 7, Moscow, Russia*

(Received 10 November 2023; revised 15 March 2024; accepted 29 April 2024; published 16 July 2024)

Here we present the nonreciprocal propagation of caustic beams and channeling of the backward volume spin wave in an yttrium-iron-garnet structure with the longitudinal symmetry axis and broken translational symmetry. The experimental method of Brillouin spectroscopy and the numerical micromagnetic methods are used to study the mechanisms of control of the nonreciprocal spin-wave signal propagation in a T-shaped junction with a partially metallized surface. It is shown that the partial metallization of the surface together with the reversal of the magnetic field direction can serve as a way to control the propagation of spin-wave beams. The formation of the spin-wave channel between the metal stripe and the edge of the magnetic film is observed experimentally and demonstrated by numerical solution of the Landau-Lifshitz-Gilbert equation and Maxwell's equations. The proposed theoretical analysis explains the experimental results and provides useful technical information for the fabrication of reconfigurable magnonic devices, which utilize the spin-wave beam formation in the region of the junction of the magnonic waveguides with different widths. The proposed structure can be used as a functional element of signal branching and/or power division in magnonic networks and signal-processing devices based on them.

DOI: 10.1103/PhysRevApplied.22.014037

## I. INTRODUCTION

The scalability of conventional CMOS-based nanoelectronics is expected to become increasingly limited over the next decade, so alternative devices beyond CMOS are being actively developed as a complement to functionally extend future nanoelectronic technology nodes [1]. A conceptual approach to information transmission and processing based on magnon principles is one of the most promising technologies. Magnons are spin-wave excitations in magnetic materials, which in the classical view can be understood as the collective precession of electron spins. The collective interaction occurs due to short-range quantum mechanical exchange interactions as well as magnetic dipole interactions [2]. In addition, spin waves (SWs) open up possibilities for the development of the wave-logic signal-processing paradigm [3], with the advantage over electromagnetic waves that even at terahertz frequencies, the wavelength of the collective spin precession can be several nanometers [4].

The energy of SWs depends substantially on the relative angle between the propagation direction and the magnetization orientation, the material parameters, and the field configuration, which is expressed in the anisotropic form of SW dispersion [5]. This anisotropic dispersion leads to the formation of nondiffracting caustic beams of SWs [6], to anomalous spin reflection, refraction and diffraction and provides different directions of group and phase velocities [7,8]. A common feature of all types of wave beams is the tendency for their transverse aperture to increase as they propagate due to the inevitable diffraction in the propagating material [8]. This effect is particularly noticeable when the initial width of the wave beam is comparable to, or even smaller than, the wavelengths forming the beam. As shown in Ref. [9], in a material with strong planar anisotropy, the diffraction of the wave beam can be reduced and the spin-wave patterns have a multibeam structure with a well-defined preferred direction of radiation. The spatial variations of the demagnetizing field lead to the complete

---

[*] Corresponding author: aamartyshkin@gmail.com

reflection of the SW in the range of nontransmission frequencies. At frequencies where the emission is resolved, rather unusual propagation features are observed due to the anisotropy of SW dispersion [10–12]. At the same time the term "superdirectional beam" could be used to show the narrowly focused nondiffracted spin-wave beam propagation similarly to the unidirectional or superdirectional light and acoustic emission process.

Signals can be encoded in the amplitude and/or phase of the SW as a unit of information using the physical wave effects in the form of a transfer of the amplitude of the angular momentum of the spins forming SW [13]. In recent years, a number of researches have been devoted to the development of SW technologies, and many goals have already been achieved in the form of SW logic gates [14], filters [15–17], delay lines [18], multiplexers [19], and spectrographs [20]. The development of the reconfigurable devices that allow the control of the direction of the spin-wave signal propagation without changing the geometry of the structure may allow more complex computational tasks to be performed without changing the configuration of the waveguides [21,22]. The building block of reconfigurable magnon circuits can be a T-shaped design based on a junction of spatially confined magnetic films in which SW beams are separated as a result of diffraction. The use of transversely confined magnetic waveguides as waveguide structures has been demonstrated in many papers, e.g., Refs. [10,23]. An obvious disadvantage of devices in which the spin-wave signal propagates along rectilinear channels is the limitation in changing the device parameters set during the design and fabrication of the waveguides. One way to increase the use of transversely constrained magnetic waveguides is to fabricate structures with broken translational symmetry [24]. Such devices can be used in different configurations of the magnetic field and the direction of propagation of the spin-wave signal, allowing them to be used in multiple modes of operation. Over the last decade, there has been an extensive study of the propagation of spin-wave caustic beams in magnetic films [9,21]. As shown in Ref. [22], caustic spin-wave beams can propagate in unpatterned magnetic films as well as being directed into formed channels. Fabricated waveguiding channels by transversely confining magnetic films allow the SW signal to be channeled [25,26].

At the same time, it has been shown that magnetostatic spin waves can propagate in magnetic films in a nonreciprocal [27,28] manner. The use of nonreciprocal effects in structures with broken translational symmetry may be another step in the creation of devices based on the principles of magnon logic. The nonreciprocal properties of magnetostatic spin waves allow us to create devices based on symmetric structures in which nonsymmetric propagation of spin waves with respect to the longitudinal symmetry axis takes place, which may be another way to control the direction of propagation of spin-wave signals in magnon logic devices [13] and spintronic devices [29].

In this paper, we investigate the nonreciprocal propagation of superdirectional quasicaustic beams of SWs in a waveguide structure with a partially metallized surface. The experimental method of Brillouin spectroscopy and numerical micromagnetic methods reveal the mechanisms of the control the spin-wave signal separation in a magnonic T-shaped junction. The transmission of the spin-wave beams is subject to being controlled by the direction of the bias magnetic field. The reversal of the magnetic field direction leads to the spatial separation of spin-wave beams in a magnonic T-shaped junction. The proposed structure can be used as a functional element of signal demultiplexing and spatial separation of the spin-wave signal in planar topologies of magnon networks and signal-processing devices based on them. The proposed structure can be used as a functional element of signal branching in planar of magnon networks and signal-processing devices based thereon.

## II. FABRICATION, EXPERIMENTAL, AND NUMERICAL METHODS

### A. Fabrication of magnonic interconnection with a metal stripe above

The structure was fabricated from single-crystal thin yttrium-iron-garnet film [YIG, $Y_3Fe_2(FeO_4)_3$ (111)] [30] with thickness $s = 10$ μm and saturation magnetization $4\pi M_s = 1750$ G. The YIG film was epitaxially grown on gallium-gadolinium-garnet substrate [GGG, $Gd_3Ga_5O_{12}$ (111)]. The ferromagnetic resonance linewidth for YIG was 0.5 Oe. Figure 1 schematically shows the T-shaped structure, which was fabricated from YIG film using the patterning with a local laser ablation system (LLAS) based on a Nd:YAG fiber laser with a two-dimensional galvanometric scanning module (Cambridge Technology 6240H) operating in a pulsed regime with a pulse duration of 50 ns and an energy of 50 mJ. The fabricated magnonic T-shape junction consists of two sections $S_1$ and $S_2$ with different widths. The input section $S_1$ formed a finite-width magnonic waveguide with the length of $l_1 = 1500$ μm and the width of $w_1 = 500$ μm. Section $S_2$ has the width of $w_2 = 6$ mm and the length of $l_2 = 4$ mm.

A microstrip antenna with a width of 25 μm was used for SW generation at the input of the $S_1$ section. At the distance $l_m = 1$ mm from the connection of sections $S_1$ and $S_2$ the $D_c = 250$-μm-width metal stripe with a thickness of 2 μm was sputtered on top of the T-shaped structure using the cold magnetron-sputtering technique [31]. Thus the fabricated structure has the longitudinal-symmetry $\xi$ axis (as shown in Fig. 1) and broken translational symmetry due to the junction of sections $S_1$ and $S_2$.

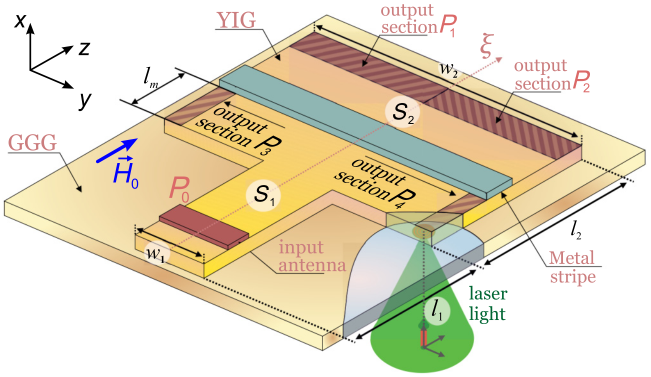

FIG. 1. Schematic of the T-shaped YIG waveguide. The curve $\xi$ denotes the longitudinal axis of symmetry of the structure consisting of two sections ($S_1$ and $S_2$) with the metal stripe on top of section $S_2$.

### B. Experimental technique and spin-wave excitation

Brillouin light-scattering (BLS) spectroscopy of magnetic materials was used to experimentally observe spin-wave propagation in the T-shaped structure with partial metallization. The method is based on the effect of inelastic light scattering from coherently excited magnons [32]. A single-frequency laser (Spectra Physics Excelsior EXLSR-532-200-CDRH) light with a wavelength of 532 nm was focused to a spot with a diameter of 25 μm and power of 1 mW on the T-shaped structure from the GGG side, as shown in Fig. 1. The microwave signal with a power level of −20 dBm from a signal generator Anritsu MG3692C was applied to the input microstrip antenna to excite the microwave magnetic field with the amplitude of about 0.1 Oe. The structure was magnetized in two different directions: positive, along the $z$ axis, and negative, antiparallel to the $z$ axis. Uniformly magnetic field generated by a GMW 3472-70 electromagnet and directed along the $z$ axis. In experiments, the value of the magnetic field was $H_0 = 1200$ Oe. An accurate positioning system was used to obtain maps of the spatial distribution of dynamic magnetization via the BLS technique. The experiment was carried out in a quasibackscattering configuration, with the intensity of the optical reflected signal being proportional to the square of the dynamic magnetization $I_{\mathrm{BLS}} \sim (m_x^2)$ in the optically probed region. Next, the stationary spatial distribution of $I_{\mathrm{BLS}}$ was obtained for different values of spin-wave input frequency. The accumulation of the BLS signal was collected in the same area of the virtual spin-wave detector, which is convenient for direct comparison with the results of the micromagnetic calculations

### C. Numerical solution of Landau-Lifshitz-Gilbert and Maxwell's equations

Micromagnetic modeling was used to solve the problem of the excitation and propagation of SWs in a microstructure [33–36]. Numerical calculations were used to simulate the transient electromagnetic wave interaction in the magnetic thin film with surface metalization by integrating the Landau-Lifshitz-Gilbert (LLG) equation within the finite-difference time-domain (FDTD) of Maxwell's equation solver [37]. This combined the electromagnetic micromagnetic approach, hereafter referred to as the FDTD-LLG method, allows the calculation of the dynamic behavior of the magnetic moments in a magnetic material subject to various micromagnetic energies (anisotropy, exchange, and external fields) while naturally evaluating the transient magnetic fields inside and outside the material from the induced magnetic charges and currents through Maxwell's equations [38]. Thus, the FDTD-LLG approach has gained increasing attention for modeling and simulation of conductive magnetic structures [39].

For a damping and dispersive material, Maxwell's equations are given by

$$\begin{cases} \frac{\partial \vec{B}}{\partial t} = -\nabla \times \vec{E}, \\ \varepsilon \frac{\partial \vec{E}}{\partial t} = \nabla \times \vec{H} - \sigma \vec{E}, \end{cases}$$

where $\vec{H}$ is the magnetic field, $\vec{E}$ is the electric field, $\varepsilon$ is the permittivity, $\sigma$ is the electrical conductivity, and $t$ is the time. The magnetic flux density $\vec{B}$ is related to the magnetization in a magnetic material through the constitutive relation: $\vec{B} = \mu_0(\vec{M} + \vec{H})$, where $\mu_0$ is the permeability of free space and $\vec{M}$ is magnetization. The LLG equation with the Gilbert-damping term was used to model the dynamic magnetization in response to an effective torque field $\vec{H}_{\mathrm{eff}}$ and is given by [40,41]

$$\frac{d\vec{M}}{dt} = -|\gamma|[\vec{M} \times \vec{H}_{\mathrm{eff}}(\vec{M})] + \frac{\alpha}{M_s}\left[\vec{M} \times \frac{d\vec{M}}{dt}\right], \quad (1)$$

where $\gamma$ is the gyromagnetic ratio, $\alpha$ is the phenomenological Gilbert-damping parameter, and $|\vec{M}| = \vec{M}_s$ is the saturation magnetization. The small deviations due to orbital contributions will not change the results and conclusions of this paper and will only lead to small shifts in the calculated resonance frequencies. The effective field is given by

$$\vec{H}_{\mathrm{eff}}(\vec{M}) = \vec{H}_0 + \vec{H}(\vec{M}) + \vec{H}_{\mathrm{ex}}(\vec{M}) + \vec{H}_{\mathrm{k}}(\vec{M}), \quad (2)$$

where $\vec{H}_0$ is the external magnetic field, $\vec{H}(\vec{M})$, the Maxwell field, $\vec{H}_{\mathrm{ex}}$, the exchange field, and $\vec{H}_{\mathrm{k}}$, the anisotropy field.

In order to reduce the SW reflections from the boundaries of the whole computational domain, an absorbing boundary condition in the form of a perfectly matched layer [37,42] with an exponentially decreasing damping parameter $\alpha$ was introduced. The excitation sources of the spin-wave signal located immediately adjacent to the absorbing boundary-layer region. At the end and both sides of the T-shaped structure, the SW detection regions were placed symmetrically with respect to the $\xi$ axis as the output sections $P_1$ and $P_2$, $P_3$ and $P_4$, as shown in Fig. 1.

The magnetization of the finite-width waveguide structure along the long axis and the propagation of spin waves collinear or noncollinear to the direction of magnetization forms the conditions for the excitation of the backward-volume magnetostatic spin waves (BVMSWs). Hence, SWs propagating in the section $S_1$ corresponded to BVMSW [43]. The input SW signal in the area of the microstrip antenna was generated by applying, along the $x$ axis, a cw magnetic field $b_0(t) = b_0 \sin(2\pi f t)$. Next, two-dimensional maps of the SW intensity distribution were constructed using the calculated dynamic magnetization components $m_{x,y,z}$ in the computational domain.

## III. RESULTS AND DISCUSSION

First we investigated the distribution of SWs in the T-shaped structure using the BLS technique. Stationary spatial distribution of $I_{\mathrm{BLS}}$ was obtained for the SW to reveal the mechanism of spin-wave transmission in the T-shaped structure at a frequency of $f = 5.15$ GHz in Figs. 2(a) and 2(b). The spatial distributions demonstrate nonsymmetrical propagation SW with respect to the longitudinal symmetry of the $\xi$ axis depending on the direction of the $H_0$. In Figs. 2(a) and 2(b), two specific regimes of SW propagation are shown: superdirected beams of spin waves propagating under and reflected from the metal stripe. The inclination of the spin-wave beam angle $\psi_\pm$ between the group velocity $\vec{V}$ and the external magnetic field $\vec{H}_0$ are schematically shown by the dashed curve. SW signal detected in the region $2.0 < z < 3.75$ mm transmitting by the superdirected beams of spin waves propagated at angles $\psi_-$ for $(y < 0)$ and $\psi_+$ for $(y > 0)$. In the other case, the spin-wave beam was reflected from the area under the metal stripe at angles $\psi_+ (y > 0)$ and $\psi_- (y < 0)$ and demonstrated the propagation of the spin-wave front along the metallized area in the range $1.0 < z < 2.0$ mm.

Furthermore, the BLS measurements were used to obtain the relative spin-wave power, which was transmitted with the spin-wave beam to the area of output antennas $P_n$, where $n$ is the port number, depicted in Fig. 1, while the exact position of these areas is shown in Fig. 2(a). Figure 2(c)–2(f) shows dimensionless parameters $P_n/P$ $(n = 1, 2, 3, 4)$ as output signal power for negative and positive directions of the uniform external magnetic field $\vec{H}_0$. The dimensionless parameters $P_n/P$

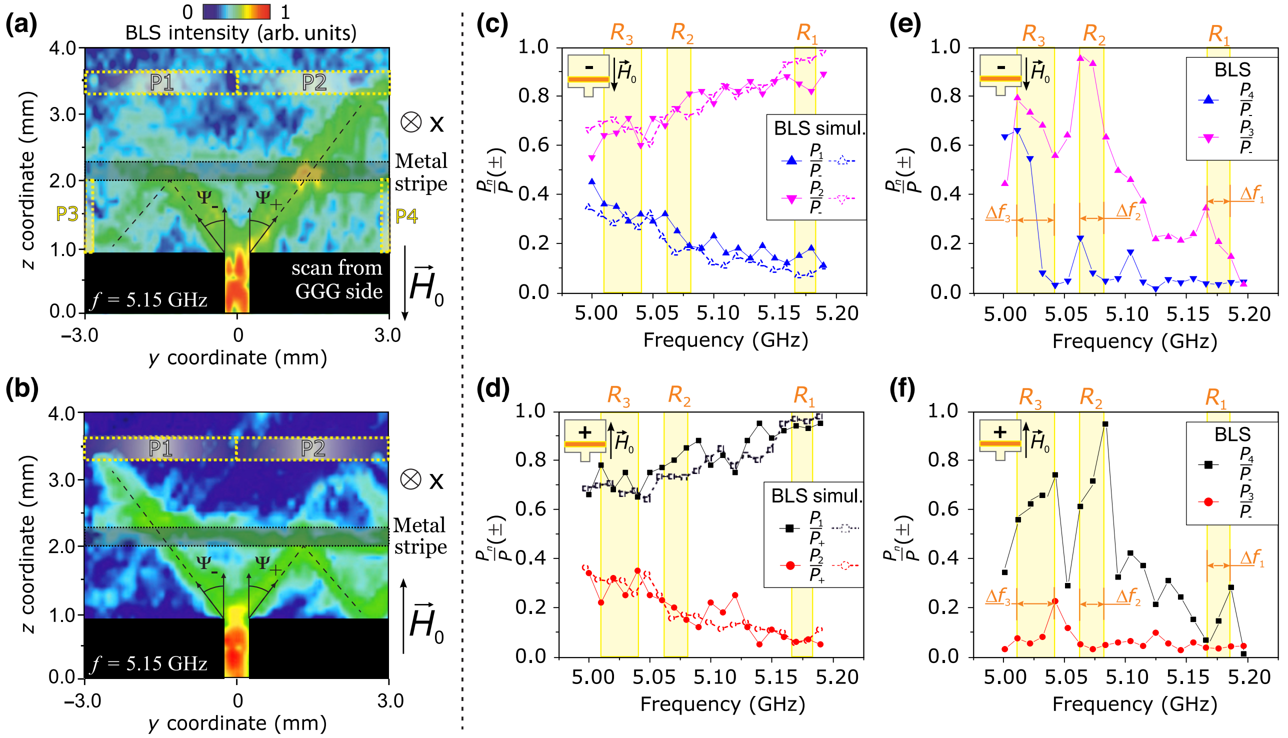

FIG. 2. Spatial distribution of the BLS signal obtained from the GGG side at the frequency $f = 5.15$ GHz for the negative (−) (a) and positive (+) (b) directions of the external magnetic field $\vec{H}_0$. Metal stripes are sputtered at the reverse side of the film. (c) Dimensionless parameters $P_n/P$ $(n = 1, 2)$ as output signal power for negative (c) and positive (d) directions of the external magnetic field $\vec{H}_0$. Dimensionless output signal power $P_n/P$ $(n = 3, 4)$ reflected from the metallized area for negative (e) and positive (f) directions of $\vec{H}_0$.

($n = 1, 2$) and $P_n/P$ ($n = 3, 4$) are the BLS signals obtained as $P = P_1 + P_2$ and $P = P_3 + P_4$, respectively. Next $P_n$ will be referred to as the BLS intensity integrated over the areas $P_n$. The size of each region (port) was $0.03 \times 3\ \mu\text{m}^2$ for $P_{1,2}$ and $1 \times 0.03\ \mu\text{m}^2$ for $P_{3,4}$. If magnetic field $\vec{H}_0$ directed along the negative orientation, the value of $P_2/P$ increases with increasing the frequency [Fig. 2(c)]. In the same time, the relative value of the power received at the output $P_2$ decreases. When the magnetic field $\vec{H}_0$ orientation is reversed the ratio $P_2/P$ decreases and $P_1/P$ increases with the frequency increase [Fig. 2(d)]. Spin-wave intensity of spin-wave beams reflected from the metallization area and propagated in the waveguide channel to the position of the output ports (antennas) $P_3$ and $P_4$ depicted in Figs. 2(e) and 2(f).

The analysis of the data provided in Figs. 2(c)–2(f) demonstrates the regime of spin-wave power division with the simultaneous outputs from both $P_2$ and $P_3$ at the $\vec{H}_0 \uparrow\downarrow z$ and from ports $P_1$ and $P_4$ at the $\vec{H}_0 \uparrow\uparrow z$. At the same time, with the increase of the input signal frequency, the intensity at side ports $P_3$ and $P_4$ decreased while the spin-wave intensity at the position of the forward ports $P_1$ and $P_2$ increased. In the case of BVMSW, the frequency increase leads to the decrease of the wave number [2,43,44], thus the observed situation corresponds to the case when the SWs with shorter wavelengths are reflected in a more pronounced way than the long wavelength signal. Figure 2(e) shows the dispersion of BVMSW [44] in the frequency range of the BLS experiment. The yellow areas in Figs. 2(c)–2(f) indicate the regions corresponding to the longitudinal wave numbers, which are $k_{zi} = i\pi/D_c$, where $i = 1, 2, 3$. This can explain the modulation of the signal intensity in Figs. 2(e) and 2(f). Thus, a more pronounced reflection occurs for wave numbers in the $k_{zi}$ range. At the same time, a possible reason for the $\Delta f_{1,2,3}$ frequency shift in the signal maxima between ports $P3$ and $P4$ is the nonreciprocal behavior of the spin-wave packet generated by the transition region between sections $S_1$ and $S_2$. A more detailed discussion of the nonreciprocal features of the spin-wave packet is given in Sec. IV.

To elucidate the formation of the waveguide channels between the edge of the YIG film and metal stripe, the micromagnetic simulations were performed. Figure 3 showed the results of the numerical simulations was performed in the MaxLLG [45]. In Ref. [41], an algorithm for calculating the discrete LLG equation was developed taking into account anisotropy and exchange fields inside the FDTD grid, which is used in the MaxLLG code. Overall experimental results are well matched by measured SW intensity maps of numerical calculations in MaxLLG. It should be noted that in Fig. 3, the $x$ axis is turned in the opposite direction, which is due to the fact that in the BLS experiment the metal stripe is on the reverse side of the magnetic film. Increasing the excitation frequency of the SW signal leads to smaller excited wavelengths in section $S_1$ and consequently to a stronger superdirected beam of the SW signal after leaving the metallized region. Excitation of the spin-wave signal at low frequencies leads to a smaller amplitude of magnetization oscillations at the $S_1$ output section (Fig. 3). This finding is consistent with the splitting trend shown in Fig. 2(c). Micromagnetic investigations agree well with the results of the BLS measurements [Fig. 2(d)] of the incident and transmitted power intensity ratio. In the simulation, the micromagnetic data were normalized to be in the same scale as the BLS data. Figure 3(e) shows the BVMSW dispersion depicted the position of frequency regions $R_1$, $R_2$, and $R_3$, where the formation of standing spin wave between the junction section and metal stripe is expected at the wave numbers $k_{z1}$, $k_{z2}$, and $k_{z3}$.

Next, we consider the symmetry of the geometrical and material parameters along with the symmetry of the profiles of spin-wave amplitudes. The term "translational symmetry" was used since the magnonic waveguide could be considered as a system that supports the propagation of spin waves along the defined $z$ direction. Waveguide could be formed as the translational motion of the rectangular cross section $s \times w_1$ along the $z$ axis. "Broken translational symmetry" means that the considered structures are formed as the junction of the two finite-width magnonic waveguide of widths $w_1$ and $w_2$ ($w_2 > w_1$). In the vicinity of the junction area, the wave packets with the transversal wave numbers $-\pi/w_1 < k_y < \pi/w_1$ are excited and propagated along the $S_2$ section. This provides the opportunity to split the spin-wave power to realize the frequency-dependent effect of spatial separation of spin-wave beams and the power division at the same time [25,26,46,47].

The structure is symmetric with respect to the longitudinal $z$ axis. In the T-shaped junction the spin-wave beam formation is observed as two separated causticlike beams, which have symmetrical intensity profiles $I(y,z) = I(-y,z)$, where $I(y,z) = \int_0^s I(x,y,z)dx$, if $y = 0$ corresponds to the position of the symmetry axis. If the bias external magnetic field is pointed along the longitudinal direction of the T-shaped junction the spin-wave amplitude profile in $x$ direction (along film thickness) is nonsymmetrical with respect to the $z$ axis [2,43]. This means that for the two spin-wave beams and observed even earlier in other experiments [25,26,46,47], the spin-wave profile $I(x,y,z)$ is nonsymmetrical with respect to the $z$ axis if the backward volume magnetostatic wave is excited in the narrow part of the T-shaped structure. Thus we have the symmetry of the structure material and geometrical parameters with respect to the $z$ axis and the asymmetry of the spin-wave profiles with respect to the same $z$ axis. If the $H$ field and average equilibrium magnetization is directed orthogonal to the symmetry $z$ axis (placed at $y = 0$) the spin-wave profiles will be symmetric $I(x,y,z) = I(x,-y,z)$. The nonreciprocal behavior manifests itself in the area where the metal stripe is placed above section $S_2$.

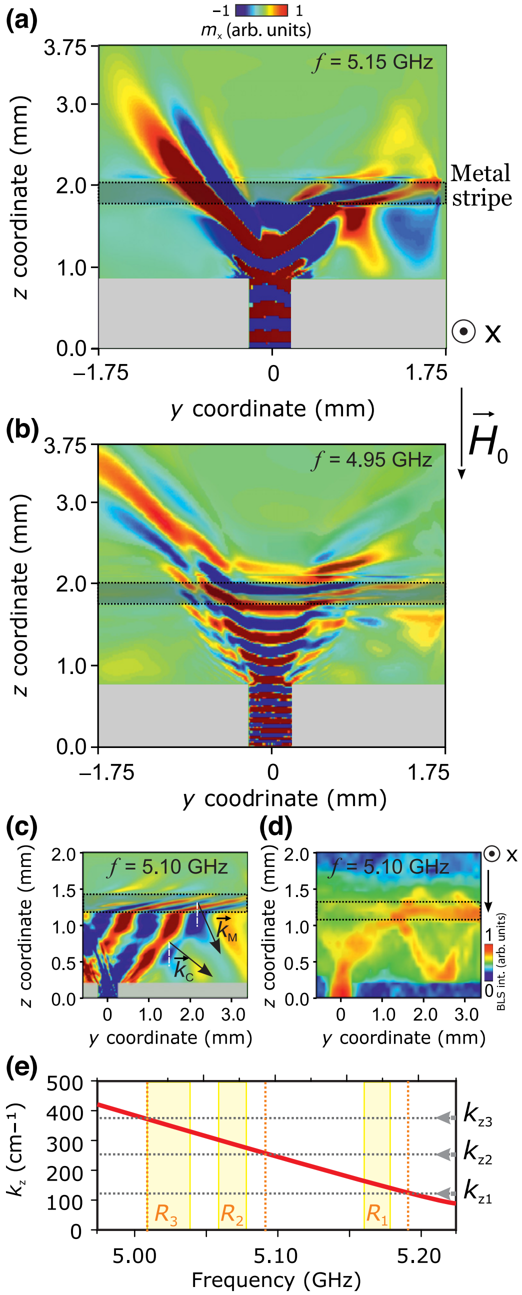

FIG. 3. Spatial distribution of intensity of the $m_x(y,z)$ component of dynamic magnetization at the negative direction of external magnetic field $\vec{H}_0$ at (a) $f = 5.15$ GHz, (b) $f = 4.95$ GHz, and (c) $f = 5.10$ GHz calculated in MaxLLG; (d) BLS map of dynamic magnetization $I(z,y)$ at $f = 5.10$ GHz demonstrating the channeling beneath the metal stripe and through the area between metal and the edge of the YIG. All data are shown for $H_0 = 1.2$ kOe; (e) dispersion of BVMSW and position of longitudinal wave numbers $k_{z1,2,3}$.

The presence of nonreciprocal effects in the studied symmetric structure leads to a mirroring of the spatial distribution of the spin-wave intensities relative to the $\xi$ axis. The asymmetric propagation of the spin-wave beams under the influence of nonreciprocity makes it possible to construct a device controlled by an external magnetic field direction in which SW propagation direction changes.

## IV. ANALYTICAL CALCULATIONS

Analytical calculations have been carried out to explain the principle of the nonreciprocal mechanism of spin-wave propagation in a partially metallized T-shaped waveguide. Isofrequency dependences (see Appendix) have been obtained for the fundamental mode of the BVMSW, when the vector of the uniform magnetic field $H_0$ is directed along the $z$ axis.

Let us consider in more detail the propagation of BVMSW at frequency $f = 5$ GHz in a T-shaped structure. Since the width of the $S_1$ section is comparable to the SW wavelength, according to the Huygens principle, a sufficiently wide set of BVMSW wave vectors $\vec{k}$ is oriented at angles $\varphi$ from the range of values $90^\circ < \varphi < 270^\circ$. These correspond to the orientation of group-velocity angles $\psi$ in the range $-43.15^\circ < \psi < 43.15^\circ$ [Figs. 4(a) and 4(b)]. Part of the energy used to excite the wave vectors $k$ near the vector $k_0$ ($\varphi = 180^\circ$), which is opposite to the $z$ axis, propagates rapidly across the film surface, since for BVMSW with wave-vector orientation $\varphi \sim 180^\circ$, the value

$$\sigma = |\frac{d\psi}{d\varphi}d\varphi|,$$

which determines the diffraction spread of the BVMSW beam, is very large [Fig. 4(c)]. It should be noted that the dependence $\psi(\varphi)$ also determines the diffraction properties of the SW wave beams, in particular, the relative angular width $\sigma$ of the SW beam according to Eq. (38) in Ref. [8]. Therefore, we cannot observe a significant concentration of the BVMSW energy in the direction of the $z$ axis: already at a distance of about 1 mm from the end of the finite-width section of the T-shaped structure, the amplitude of the BVMSW is small, as can be seen in Figs. 2(a) and 2(b).

The superdirectional propagation of BVMSW is realized with wave vector $\vec{k}$ oriented at angles $\varphi_{s2} = 156.2^\circ$ and $\varphi_{s3} = -156.2^\circ$ in directions $\psi_{s2} = 43.15^\circ$ and $\psi_{s3} = -43.15^\circ$, respectively. Spin-wave propagation occurs in the directions $\psi_{s2} = 43.15^\circ$ and $\psi_{s3} = -43.15^\circ$, because when $\varphi_{s2}$ and $\varphi_{s3}$ wave vectors $k_{s2}$ and $k_{s3}$ are oriented, the value of the relative angular width $\sigma = 0$ [Figs. 4(b) and 4(c)]. This fact significantly affects the propagation of the excited wave beams of the BVMSW: due to the absence of diffraction divergence, the energy of the BVMSW is localized in the $\psi_{s3}$ and $\psi_{s3}$ directions emanating from the border $S_1$, and practically not unfocused [see Figs. 2(a) and 2(b)] as in Ref. [48]. Note here that at the inflection points of the isofrequency dependence, the group-velocity vectors $V_{s2}$ and $V_{s3}$ deviate from the external magnetic field vector $\vec{H}_0$ by the maximum possible angles $\psi_{s2}$ and $\psi_{s3}$ (exceeding the cutoff angles), and therefore the entire energy of

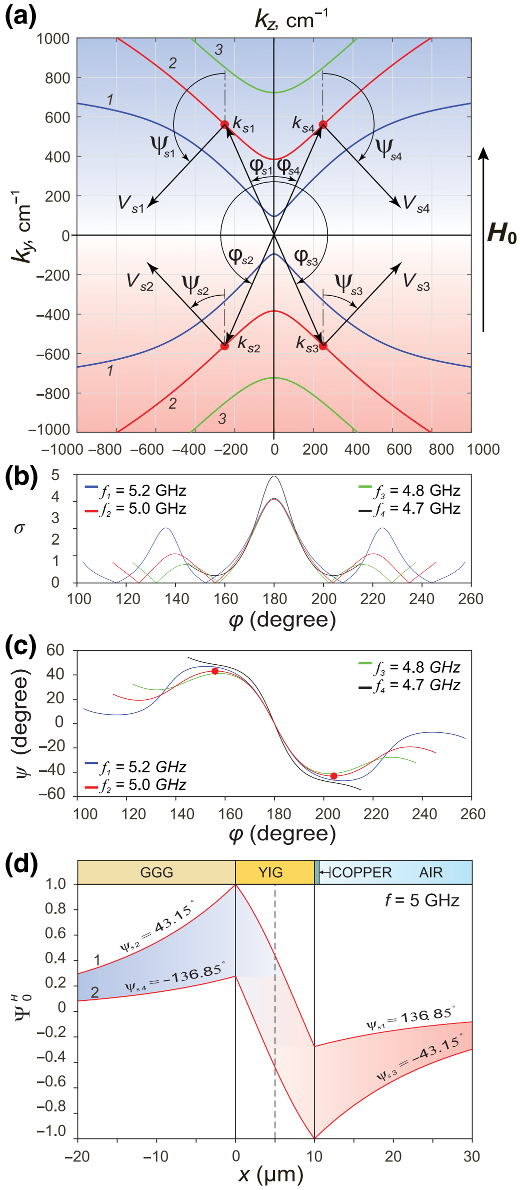

FIG. 4. Theoretical calculation: (a) isofrequency dependencies; (b) dependences of the angle $\psi$, at which the group-velocity vector $V$ is oriented, on the angle $\varphi$ setting the orientation of the wave vector $k$ of the BVMSW. Red dots indicate the wave parameters at which $d\psi/\varphi = 0$ at frequency $f = 5.0$ GHz; (c) the dependences of the relative angular width of the BVMSW wave beam $\sigma$ on angle $\varphi$ for the BVMSW; (d) the normalized distribution of the magnetic potential amplitude $\Psi^n_{j0}(x)$ for wave beams of the first mode of the BVMSW. $x = 0, x = s/2 = 5$ μm, and $x = s = 10$ μm coordinates, corresponding to surfaces, middle and end of the ferrite film.

the BVMSWs excited at a frequency of $f = 5$ GHz in the range of angles $-43.15° < \psi < 43.15°$, which corresponds well to the energy distribution of the BVMSW observed in the BLS experiment.

Next we consider the spin-wave beams, which could be referred to as quasi-BVMSW beams, and propagates at angles $\psi_{s2}$ and $\psi_{s3}$, which satisfies the condition:

$$|\varphi_{s2}| = |\varphi_{s3}|, \quad |\psi_{s2}| = |\psi_{s3}|, \quad k_{s2} = k_{s3}, \quad V_{s2} = V_{s3}.$$

These wave beams are characterized by the normalized distribution of the magnetic potential amplitude $\Psi^H_{j0}(x)$ in the cross section of the film for each of these beams has the largest maximum at different surfaces of the YIG film [Fig. 4(d)] [28,49]. This means that the main part of the energy of the wave beam propagating in the direction $\psi_{s2} = 43.15°$ is localized near the lower surface of the ferrite film at the YIG-GGG interface [see curve 1 in Fig. 4(d)]. At the same time, the main part of the energy of the wave beam propagating in the direction $\psi_{s3} = -43.15°$ is near the upper surface of the ferrite film [YIG-metal interface, see curve 2 in Fig. 4(d)].

Let us now consider the characteristics of the BVMSW for the case where the vector of the external magnetic field $H_0$ is directed opposite to the $z$ axis. When the $H_0$ direction changes, the same calculations could be carried out, in which a different magnetic permeability tensor would be used (with the field $H_0$ directed opposite to the $z$ axis), as shown in Ref. [28,49]. However, it is easier to do otherwise: we can assume that the characteristics of the geometry, in which the vector $H_0$ is directed opposite to the $z$ axis, are obtained as a result of rotating the isofrequency dependences of the BVMSW (together with the vector $\vec{H_0}$) around the coordinate center per 180°. In the same coordinate axis $(k_y, k_z)$, the rotation of the isofrequency curves [Fig. 4(a)] leads to the isofrequency configuration describing this geometry.

As a result of such a rotation, the place of the wave vectors $k_{s2}$ and $k_{s3}$ and the group-velocity vectors $V_{s2}$ and $V_{s3}$ will be occupied, respectively, by the vectors $k_{s4}$, $k_{s1}$, and $V_{s4}$, $V_{s1}$, which (together with their orientations $\varphi_{s4}$, $\varphi_{s1}$, $\psi_{s4}$, and $\psi_{s1}$) will now determine the properties of superdirectional wave beams excited by the junction between $S_1$ and $S_2$ sections of the T-shaped structure. In the direction $\psi = 43.15°$ denoted in Fig. 2(b) a superdirectional wave beam is propagated. In this case, the normalized distribution of the magnetic potential amplitude $\Psi^n_{j0}(x)$ determines the angle $\varphi_{s4} = -23.8°$ and therefore the main part of the energy of this beam will be localized near the upper surface of the film at the YIG-metal interface [curve 2 in Fig. 4(d)]. Similarly, in the direction $\psi = -43.15°$ in Fig. 2(b) a superdirectional wave beam is propagated, with the distribution $\Psi^n_{j0}(x)$ determines the angle $\varphi_{s1} = 23.8°$, and the main part of the energy of this beam will be localized near the bottom surface of the ferrite film [see curve 1 in Fig. 4(d)]. Thus, the analysis presented above showed that superdirectional wave beams propagating in the same directions ($\psi = \pm 43.15°$) on Figs. 2(a) and 2(b) differ significantly in the distribution of the magnetic potential $\Psi^n(x)$, the largest maximum of which is localized at different surfaces of the ferrite film.

In order to consider theoretically what happens when superdirectional wave beams reach a metal stripe, let us recall some of the previously discovered properties of the BVMSW. Thus, in the paper [50] it was shown that an electromagnetic wave, known in the description in the magnetostatic approximation as BVMSW, has all six components of the microwave electromagnetic field—three electric $E_x$, $E_y$, $E_z$ and three magnetic $H_x$, $H_y$, $H_z$ both in the ferrite layer and in adjacent half-spaces: in other words, as a result of satisfying the boundary conditions on the surface of the ferrite, both the $E$ wave and the $H$ wave arise in the adjacent half-spaces, which are coupled to each other through the ferrite plate. Although the paper [50] considered only the case of propagation of this wave along the vector $\vec{H}_0$, it is obvious that waves propagating in other directions (in particular, the superdirectional wave beams studied here) have three magnetic and three electric components of the microwave field. Based on these results, we can assume that when a wave beam approaches the metallized part of the ferrite-film surface, in which the main part of the energy is localized near the same surface (i.e., this film surface has tangential electrical components of the wave $E_y$ and $E_z$), then the main part of the wave energy is reflected from the ferrite-ferrite and metal-junction section back into the nonmetallized part of the film. If, on the other hand, a wave beam approaches the metallized part of the surface of the ferrite film, in which the main part of the energy is localized at the opposite (nonmetallized) surface [and the tangential electrical components of the waves $E_y$ and $E_z$ are sufficiently small near the metallized surface of the film, by analogy with the dependence $\Psi^n_{j0}(x)$], then the main part of the wave energy passes unhindered under the metal stripe and propagates further, and the wave reflections from the ferrite-ferrite and metal-junction section in this case practically do not occur.

## V. CONCLUSION

In conclusion, the nonreciprocal propagation of spin-wave caustic beams in a waveguide structure with a partially metallized surface was studied. It is shown that nonreciprocal effects can find an alternative application in the control of spin-wave signals in magnon logic devices based even on the structures with the longitudinal symmetry axis and broken translational symmetry. At first glance, the nonreciprocal propagation is forbidden for the excited backward-volume spin wave in YIG even with the metallization of one of the film surfaces in contrast to the case of the surface spin wave excited in Damon-Eshbach geometry [2,5,43,51] but the observed spin-wave propagation regime demonstrates a clearly defined nonsymmetrical behavior with the symmetry axis of the structure.

The experimental method of Brillouin spectroscopy and the numerical simulation method show the mechanisms of controlling the spin-wave signal in a T-shaped junction. The analytical estimation of the spin-wave beam group-velocity direction and the wave profile elucidate the reflection mechanism of spin-wave-beam and explains the nonreciprocal behavior of the spin-wave demultiplexer regime. It is shown that partial surface metallization can provide a tunable magnonic beam-splitter element based on the spin-wave caustics separation. Moreover, the unidirectional channeling of spin waves in the region between the metallized layer and the edge of the magnon plate allows the realization of the regime of signal propagation in the direction orthogonal to the initial direction of spin wave. The proposed structure can be used as a functional element of signal separation and channeling in planar topologies of magnonic networks.

The data that support the findings of this study are available upon request from the authors. Interested readers can reproduce results of magnetic structure simulation by using the version of software at Ref. [45].

## ACKNOWLEDGMENTS

Brillouin light-scattering measurements and the spin-wave beam-formation study were supported by Russian Science Foundation (Grant No. 20-79-10191). The FDTD-LLG approach for simulation of conductive magnetic structures was performed with MaxLLG with the support of EU H2020-MSCA-RISE projects TERASSE (Project No. 823878) and DiSeTCom (Project No. 823728). E.H.L. performed his work as part of State Task of Kotel’nikov Institute of Radio Engineering and Electronics of Russian Academy of Sciences.

## APPENDIX

### 1. Diffraction divergence of the spin-wave beam and isofrequency characteristics

The dispersion equation describing the BVMSW modes [Eq. (6) in Ref. [8]] in a free ferrite film in the polar coordinates could be set as

$$k = \frac{1}{\alpha s}\left[(n-1)\pi + \operatorname{arcctg}\left(\frac{1/\mu + \cos^2\varphi + \mu_\perp \sin^2\varphi}{-2\alpha}\right)\right], \tag{A1}$$

where $\mu_\perp = (\mu^2 - \nu^2)/\mu$, $\mu = 1 + \omega_M\omega_H/(\omega_H^2 - \omega^2)$, and $\nu = \omega_M\omega/(\omega_H^2 - \omega^2)$ are components of the magnetic permeability tensor of ferrite, $\omega_H = \gamma H_0$, $\omega_M = 4\pi\gamma M_0$, $\omega = 2\pi f$, $\gamma$ are the gyromagnetic constants, $H_0$ is the uniform magnetic field, $4\pi M_0$ is the saturation magnetization, $\alpha = \sqrt{-\cos^2\varphi/\mu - \sin^2\varphi}$, $\varphi$ is the angle between $\vec{k}$ and the $z$ axis, and $n$ is the mode number ($n = 1, 2, 3, \ldots$).

Based on Eq. (A1), the isofrequency dependence $k(\varphi)$ can be calculated explicitly for the BVMSW with any fixed frequency $f$. At the same time, in the Cartesian coordinate system $k_y = -k\sin\varphi$, $k_z = k\cos\varphi$ the isofrequency dependence $k_z(k_y)$ could be obtained. Figure 4(a) shows the isofrequency dependences for the first mode of BVMSW calculated by Eq. (A1) for different frequencies at the orientation of the homogeneous magnetic field vector $H_0$ along the $z$ axis.

From the isofrequency dependences shown in Fig. 4(a), it is impossible to determine precisely the angle $\psi$ between the group-velocity vector $v$ and the $z$ axis (this angle determines the direction of energy transfer by the wave beam). It is known that this angle, described by the expression,

$$\psi = \mathrm{arctg}\frac{\partial k_z}{\partial k_y} + n\pi, \tag{A2}$$

can be calculated using Eqs. (20)–(24) given in Ref. [49]. Note that at $n = 0$ the values of $\psi$ will correspond to the isofrequency curves lying below the $k_y$ axis in Fig. 4(a), and at $n = 1$, the isofrequency curves lying above the $k_y$ axis. The calculated dependences of $\psi(\varphi)$ corresponding to the isofrequency dependences in Fig. 4(a) are shown in Fig. 4(b).

As shown in Ref. [8], the dependence $\psi(\varphi)$ also determines the diffraction properties of SW beams. In particular, the angular width of the beam in an anisotropic medium $\Delta\psi_{\mathrm{anis}}$ determined by the formula (see Sec. 9 in Ref. [8])

$$\Delta\psi_{\mathrm{anis}} = \frac{\lambda_0}{D}\left|\frac{d\psi}{d\varphi}(\varphi_0)\right|, \tag{A3}$$

where $D$ is the length of the exciter (e.g., the transducer exciting the SW), $\lambda_0$ is the length of the excited SW, and a is the curvature of the isofrequency dependence at the point to which vector $\vec{k}$, oriented at an angle $\varphi_0$, is directed. In isotropic media, where the isofrequency dependence of the wave is a circle, and the vector $\vec{k}$ and the corresponding vector $\vec{V}$ (the normal line of the circle) are always co-directional, the dependence $\psi(\varphi)$ has the form $\psi = \varphi$, and, therefore, the relation $\psi/\varphi \equiv 1$ is satisfied. Thus, for isotropic media, expression (A3) transforms into

$$\Delta\psi_{\mathrm{isotr}} = \frac{\lambda_0}{D}, \tag{A4}$$

which defines the Rayleigh solvability criterion and is used to estimate the angular width of a beam (of light or other waves) in isotropic media. The degree of diffraction divergence of a beam in an anisotropic medium is conveniently characterized by calculating the value $\sigma$

$$\sigma = \frac{\Delta\psi_{\mathrm{anis}}}{\Delta\psi_{\mathrm{isotr}}} = \frac{\Delta\psi_{\mathrm{anis}}}{\lambda_0/D} = \left|\frac{d\psi}{d\varphi}(\varphi_0)\right|. \tag{A5}$$

In the physical sense, the value $\sigma$, defined by formula (A5), is the relative angular width of the diffraction ray and shows how many times the angular width $\Delta\psi_{\mathrm{anis}}$ of some ray in an anisotropic medium is larger or smaller than the width $\Delta\psi_{\mathrm{isotr}}$ of a similar ray (with the same $\lambda_0/D$ ratio) in an isotropic medium. As can be seen, the value of $\sigma$ depends only on the curvature of the isofrequency dependence of the wave $d\psi/d\varphi$. Since for isotropic media $d\psi/d\varphi \equiv 1$, it follows from Eq. (A5) that for these media $\sigma_{\mathrm{isotr}} \equiv 1$. Therefore, to estimate the degree of diffraction divergence of a ray in an anisotropic medium, it is enough to compare the value $\sigma$ calculated for it with unity: how many times $\sigma$ will be greater (or less) than unity, so many times the diffraction divergence of the ray will be greater (or less) than in isotropic media.

The calculated dependencies $\sigma(\varphi)$ corresponding to the dependencies in Figs. 4(a) and 4(b) are presented in Fig. 4(c).

### 2. Profile of the magnetic potential

Also, in the further analysis, we need to calculate the distribution of the magnetic potential of the BVMSW $\Psi$ (which determines the energy distribution of the BVMSW) along the $x$ axis perpendicular to the plane of the ferrite film. As is known, the magnetic potential of the BVMSW $\Psi_j$ inside and outside the film ($j = 1, 2$, or 3) can be written in the form $\Psi_j = \Psi_{j0}\exp(-ikr)$, and the amplitudes of the potential $\Psi_{j0}$ in each medium describe the expressions [see Eq. (7) in Ref. [28]]:

$$\begin{aligned}\Psi_{10} &= B\left[\frac{1+\nu\sin\varphi}{\alpha\mu}\sin(\alpha ks) + \cos(\alpha ks)\right]\exp(ks - kx),\\ \Psi_{20} &= B\left[\frac{1+\nu\sin\varphi}{\alpha\mu}\sin(\alpha kx) + \cos(\alpha kx)\right],\\ \Psi_{30} &= B\exp(ks - kx),\end{aligned} \tag{A6}$$

where $B$ is an arbitrary coefficient (which can be set equal to one). The dependence of the normalized amplitude of potentials on the coordinate $x$ will be calculated by the formula

$$\Psi^n_{j0}(x) = \Psi_{j0}/(\Psi_{20\max}), \tag{A7}$$

where $\Psi_{20\max}$ is the maximum value of the $|\Psi_{20\max}|$ in the range $0 < x < s$ (see Ref. [50] for details). Expressions (A6) and (A7) allow us to calculate the dependence for fixed values of $f$, $k$, and $\varphi$ satisfying the dispersion equation, Eq. (A1).

[1] A. Barman, *et al.*, The 2021 magnonics roadmap, J. Phys.: Condens. Matter **33,** 413001 (2021).

[2] D. D. Stancil and A. Prabhakar, *Spin Waves: Theory and Applications* (Springer, New York, 2009).

[3] P. Pirro, V. I. Vasyuchka, A. A. Serga, and B. Hillebrands, Advances in coherent magnonics, Nat. Rev. Mater. **6**, 1114 (2021).

[4] S. A. Nikitov, A. R. Safin, D. V. Kalyabin, A. V. Sadovnikov, E. N. Beginin, M. V. Logunov, M. A. Morozova, S. A. Odintsov, S. A. Osokin, and A. Y. Sharaevskaya, *et al.*, Dielectric magnonics: From gigahertz to terahertz, Phys.-Usp. **63**, 945 (2020).

[5] R. Damon and J. Eschbach, Magnetostatic modes of a ferromagnet slab, J. Phys. Chem. Solids **19**, 308 (1961).

[6] A. V. Chumak, Fundamentals of magnon-based computing, ArXiv:1901.08934.

[7] V. Veerakumar and R. E. Camley, Magnon focusing in thin ferromagnetic films, Phys. Rev. B **74**, 214401 (2006).

[8] E. H. Lock, Angular beam width of a slit-diffracted wave with noncollinear group and phase velocities, Usp. Fizich. Nauk **182**, 1327 (2012).

[9] T. Schneider, A. A. Serga, A. V. Chumak, C. W. Sandweg, S. Trudel, S. Wolff, M. P. Kostylev, V. S. Tiberkevich, A. N. Slavin, and B. Hillebrands, Nondiffractive subwavelength wave beams in a medium with externally controlled anisotropy, Phys. Rev. Lett. **104**, 197203 (2010).

[10] V. E. Demidov, S. O. Demokritov, D. Birt, B. O'Gorman, M. Tsoi, and X. Li, Radiation of spin waves from the open end of a microscopic magnetic-film waveguide, Phys. Rev. B **80**, 014429 (2009).

[11] S. Mamica, M. Krawczyk, and D. Grundler, Nonuniform spin-wave softening in two-dimensional magnonic crystals as a tool for opening omnidirectional magnonic band gaps, Phys. Rev. Appl. **11**, 054011 (2019).

[12] P. Gruszecki, K. Y. Guslienko, I. L. Lyubchanskii, and M. Krawczyk, Inelastic spin-wave beam scattering by edge-localized spin waves in a ferromagnetic thin film, Phys. Rev. Appl. **17**, 044038 (2022).

[13] A. V. Chumak, P. Kabos, M. Wu, C. Abert, C. Adelmann, A. Adeyeye, J. Åkerman, F. G. Aliev, A. Anane, and A. Awad, *et al.*, Advances in magnetics roadmap on spin-wave computing, IEEE Trans. Magn. **58**, 1 (2022).

[14] A. Kolosvetov, M. Kozhaev, I. Savochkin, V. Belotelov, and A. Chernov, Concept of the optomagnonic logic operation, Phys. Rev. Appl. **18**, 054038 (2022).

[15] B. G. Simon, S. Kurdi, J. J. Carmiggelt, M. Borst, A. J. Katan, and T. Van Der Sar, Filtering and imaging of frequency-degenerate spin waves using nanopositioning of a single-spin sensor, Nano Lett. **22**, 9198 (2022).

[16] G. Gubbiotti, A. Sadovnikov, E. Beginin, S. Sheshukova, S. Nikitov, G. Talmelli, I. Asselberghs, I. P. Radu, C. Adelmann, and F. Ciubotaru, Magnonic band structure in CoFeB/Ta/NiFe meander-shaped magnetic bilayers, Appl. Phys. Lett. **118**, 162405 (2021).

[17] G. Gubbiotti, A. Sadovnikov, E. Beginin, S. Nikitov, D. Wan, A. Gupta, S. Kundu, G. Talmelli, R. Carpenter, I. Asselberghs, I. P. Radu, C. Adelmann, and F. Ciubotaru, Magnonic band structure in vertical meander-shaped $\mathrm{Co_{40}Fe_{40}B_{20}}$ thin films, Phys. Rev. Appl. **15**, 014061 (2021).

[18] A. Liu and A. M. Finkel'stein, Control of spin waves by spatially modulated strain, Phys. Rev. B **105**, L020404 (2022).

[19] A. Grachev, S. Sheshukova, M. Kostylev, S. Nikitov, and A. Sadovnikov, Reconfigurable dipolar spin-wave coupling in a bilateral yttrium iron garnet structure, Phys. Rev. Appl. **19**, 054089 (2023).

[20] Á. Papp, W. Porod, Á. I. Csurgay, and G. Csaba, Nanoscale spectrum analyzer based on spin-wave interference, Sci. Rep. **7**, 9245 (2017).

[21] O. Dzyapko, I. V. Borisenko, V. E. Demidov, W. Pernice, and S. O. Demokritov, Reconfigurable heat-induced spin wave lenses, Appl. Phys. Lett. **109**, 232407 (2016).

[22] F. Heussner, A. A. Serga, T. Brächer, B. Hillebrands, and P. Pirro, A switchable spin-wave signal splitter for magnonic networks, Appl. Phys. Lett. **111**, 122401 (2017).

[23] K. Vogt, F. Fradin, J. Pearson, T. Sebastian, S. Bader, B. Hillebrands, A. Hoffmann, and H. Schultheiss, Realization of a spin-wave multiplexer, Nat. Commun. **5**, 3727 (2014).

[24] A. Martyshkin, C. Davies, and A. Sadovnikov, Magnonic interconnections: Spin-wave propagation across two-dimensional and three-dimensional junctions between yttrium iron garnet magnonic stripes, Phys. Rev. Appl. **18**, 064093 (2022).

[25] T. Brächer, P. Pirro, J. Westermann, T. Sebastian, B. Lägel, B. Van de Wiele, A. Vansteenkiste, and B. Hillebrands, Generation of propagating backward volume spin waves by phase-sensitive mode conversion in two-dimensional microstructures, Appl. Phys. Lett. **102**, 132411 (2013).

[26] A. V. Sadovnikov, C. S. Davies, S. V. Grishin, V. V. Kruglyak, D. V. Romanenko, Y. P. Sharaevskii, and S. A. Nikitov, Magnonic beam splitter: The building block of parallel magnonic circuitry, Appl. Phys. Lett. **106**, 192406 (2015).

[27] R. Gallardo, T. Schneider, A. Chaurasiya, A. Oelschlägel, S. Arekapudi, A. Roldán-Molina, R. Hübner, K. Lenz, A. Barman, J. Fassbender, J. Lindner, O. Hellwig, and P. Landeros, Reconfigurable spin-wave nonreciprocity induced by dipolar interaction in a coupled ferromagnetic bilayer, Phys. Rev. Appl. **12**, 034012 (2019).

[28] E. Lock, Nonreciprocal properties of the backward spin waves, J. Commun. Technol. Electron. **65**, 265 (2020).

[29] B. Dieny, *et al.*, Opportunities and challenges for spintronics in the microelectronics industry, Nat. Electron. **3**, 446 (2020).

[30] CJSC NII Materialovedenie, Zelenograd, Russia.

[31] J. T. Gudmundsson, Physics and technology of magnetron sputtering discharges, Plasma Sources Sci. Technol. **29**, 113001 (2020).

[32] S. Demokritov, Brillouin light scattering studies of confined spin waves: Linear and nonlinear confinement, Phys. Rep. **348**, 441 (2001).

[33] D. M. Pozar, *Microwave Engineering* (John Wiley & Sons, Hoboken, 2012), 4th ed.

[34] A. V. Sadovnikov, C. S. Davies, V. V. Kruglyak, D. V. Romanenko, S. V. Grishin, E. N. Beginin, Y. P. Sharaevskii, and S. A. Nikitov, Spin wave propagation in a uniformly biased curved magnonic waveguide, Phys. Rev. B **96**, 060401(R) (2017).

[35] A. V. Sadovnikov, A. A. Grachev, E. N. Beginin, S. E. Sheshukova, Y. P. Sharaevskii, and S. A. Nikitov, Voltage-controlled spin-wave coupling in adjacent

ferromagnetic-ferroelectric heterostructures, Phys. Rev. Appl. **7**, 014013 (2017).

[36] A. V. Sadovnikov, A. A. Grachev, S. E. Sheshukova, Y. P. Sharaevskii, A. A. Serdobintsev, D. M. Mitin, and S. A. Nikitov, Magnon straintronics: Reconfigurable spin-wave routing in strain-controlled bilateral magnetic stripes, Phys. Rev. Lett. **120**, 257203 (2018).

[37] A. Taflove and S. Hagness, *Computational Electrodynamics: The Finite-Difference Time-Domain Method* (Arctech House, Boston, MA, 2000), 2nd ed.

[38] M. Aziz and C. McKeever, Wide-band electromagnetic wave propagation and resonance in long cobalt nanoprisms, Phys. Rev. Appl. **13**, 034073 (2020).

[39] Z. Yao, R. U. Tok, T. Itoh, and Y. E. Wang, A multiscale unconditionally stable time-domain (must) solver unifying electrodynamics and micromagnetics, IEEE Trans. Microw. Theory Tech. **66**, 2683 (2018).

[40] W. Brown and E. Robert, *Micromagnetics* (Krieger Publishing Co., New York, 1978).

[41] M. M. Aziz, Sub-nanosecond electromagnetic-micromagnetic dynamic simulations using the finite-difference time-domain method, Prog. Electromagn. Res. B **15**, 1 (2009).

[42] G. Venkat, H. Fangohr, and P. A., Absorbing boundary layers for spin wave micromagnetics, J. Mag. Magn. Mater. **450**, 34 (2018).

[43] A. G. Gurevich and G. A. Melkov, *Magnetization Oscillations and Waves* (CRC Press, London, New York, 1996).

[44] B. A. Kalinikos and A. N. Slavin, Theory of dipole-exchange spin wave spectrum for ferromagnetic films with mixed exchange boundary conditions, J. Phys. C: Solid State Phys. **19**, 7013 (1986).

[45] *High Frequency Magnetics Software [Electronic Resource]* (Maxllg, Innovation Centre, University of Exeter, Devon, UK, 2019), available from https://www.maxllg.com.

[46] A. V. Vashkovskii, V. S. Stalmakhov, and Y. P. Sharaevskii, *Magnetostatic Waves in Microwave Electronics* (Sarat. Gos. Univ., Saratov, 1993), (in Russian).

[47] A. V. Vashkovskii and E. H. Lokk, Negative refractive index for a surface magnetostatic wave propagating through the boundary between a ferrite and ferrite-insulator-metal media, Phys.-Usp. **47**, 601 (2004).

[48] A. Annenkov, S. Gerus, and E. Lock, Superdirected beam of the backward volume spin wave, EPJ Web Conf. **185**, 02006 (2018).

[49] A. Vashkovksii and E. Lock, Properties of backward electromagnetic waves and negative reflection in ferrite films, PhyS.-Usp. **49**, 389 (2006).

[50] A. Vashkovksii and E. Lock, The physical properties of a backward magnetostatic wave described on the basis of the Maxwell equations, J. Commun. Technol. Electron. **57**, 490 (2012).

[51] T. W. O'Keeffe and R. W. Patterson, Magnetostatic surface-wave propagation in finite samples, J. Appl. Phys. **49**, 4886 (1978).